Journal Pre-proofs

Interfacial Separation of Concentrated Dye Mixtures from Solution with Environmentally Compatible Nitrogenous-Silane Nanoparticles modified with Helianthus annuus Husk Extract

Adam Truskewycz, Mohamed Taha, Deshetti Jampaiah, Ravi Shukla, Andrew S. Ball, Ivan Cole

Please cite this article as: A. Truskewycz, M. Taha, D. Jampaiah, R. Shukla, A.S. Ball, I. Cole, Interfacial Separation of Concentrated Dye Mixtures from Solution with Environmentally Compatible Nitrogenous-Silane Nanoparticles modified with Helianthus annuus Husk Extract, *Journal of Colloid and Interface Science* (2019), doi: https://doi.org/10.1016/j.jcis.2019.10.108

Interfacial Separation of Concentrated Dye Mixtures from Solution with Environmentally Compatible Nitrogenous-Silane Nanoparticles modified with Helianthus annuus Husk Extract

Adam Truskewycz[a,d]*, Mohamed Taha[a,b] , Deshetti Jampaiah[c], Ravi Shukla[a,c], Andrew S. Ball[a], Ivan Cole[d]

[a] Centre for Environmental Sustainability and Remediation, School of Science, RMIT University, Bundoora, VIC 3083, Australia

[b] Department of Biochemistry, Faculty of Agriculture, Benha University, Moshtohor, Toukh, Qaliuobia 13736, Egypt

[c] Nanobiotechnology Research Laboratory and Centre for Advanced Materials & Industrial Chemistry, School of Science, RMIT University, Melbourne, VIC 3000, Australia

[d] Advanced Manufacturing and Fabrication, School of Engineering, RMIT University, Melbourne, VIC 3000, Australia

Corresponding Author: Adam Truskewycz, adam.truskewycz@rmit.edu.au/ +61 423744356/ SEH College Common Store 201.01.05, Bundoora West Campus RMIT University, Plenty Road Bundoora VIC, Australia, 3083

1

Interfacial Separation of Concentrated Dye Mixtures from Solution with Environmentally Compatible Nitrogenous-Silane Nanoparticles modified with *Helianthus annuus* Husk Extract

Adam Truskewycz[a,d]*, Mohamed Taha[a,b], Deshetti Jampaiah[c], Ravi Shukla[a,c], Andrew S. Ball[a], Ivan Cole[d]

[a] Centre for Environmental Sustainability and Remediation, School of Science, RMIT University, Bundoora, VIC 3083, Australia

[b] Department of Biochemistry, Faculty of Agriculture, Benha University, Moshtohor, Toukh, Qaliuobia 13736, Egypt

[c] Nanobiotechnology Research Laboratory and Centre for Advanced Materials & Industrial Chemistry, School of Science, RMIT University, Melbourne, VIC 3000, Australia

[d] Advanced Manufacturing and Fabrication, School of Engineering, RMIT University, Melbourne, VIC 3000, Australia

Abstract

The capacity of an adsorbent to bind and remove dye from solution greatly depends on the type of functionalization present on the nanoparticles surface, and its interaction with the dye molecules. Within this study, nitrogenous silane nanoparticles were hydrothermally synthesized resulting in the formation of rapid and highly efficient adsorbents for concentrated mixed dyes. The amorphous silane nanoparticles exhibited a monolayer based mechanism of mixed dye adsorption with removal capacities between 416.67 – 714.29 mg/ g of adsorbent. Dye removal was predominantly due to the electrostatic attraction between the positively charged silane nanoparticles (13.22- 8.20 mV) and the negatively charged dye molecules (-54.23 mV). Addition of *H. annuus* extract during synthesis resulted in three times the surface area and 10 times increased pore volume compared to the positive control. XPS analysis showed that silane treatments had various nitrogen containing

functionalities at their surface responsible for binding dye. The weak colloidal stability of silane particles (13.22 - 8.20 mV) was disrupted following dye binding, resulting in their rapid coagulation and flocculation which facilitated the separation of bound dye molecules from solution. The suitability for environmental applications using these treatments was supported by a bacterial viability assay showing > 90% cell viability in treated dye supernatants.

Key Words: Porous; APTES; Nanoparticles; Adsorption; Interfacial, Colloidal stability

1. Introduction

Dyes are a valuable commodity, with global production of dyestuffs currently exceeding 7×10^5 t annually [1, 2]. This figure is only set to rise with global population growth and increased consumer demand for textile goods. However, the environmental persistence and inherent toxicity of dyestuffs is of increasing concern. For example, hydrolysed remazol brilliant blue, a commonly used dye has been shown to possess high aqueous solubility, high toxicity and contains an electrophilic vinyl-sulfone group capable of causing mutagenic effects. This dye has a half-life of 46 years at 25°C [3-5].

Among all dyes used within the textile industry, 10-15% are found in post-dye wastewater, many of which have the potential to cause serious environmental and socio-economic damage [1]. China, the world's leading exporter of dyestuff passed legislation in 2003 requiring cleaner production and less environmentally damaging approaches to the manufacture of dyes (Law of the People's Republic of China on Promotion of Cleaner Production)[6]. Similar legislation exists around the world prompting the need for the development of innovative methods for the minimization of dye-pollution and subsequent remediation strategies.

Currently, adsorption is the most widely used treatment option for dye remediation from wastewater as it is economically practical, fast, effective and removes dye molecules without breaking their structure into smaller toxic daughter products [7]. Functionalization of adsorbents is often required for elevated dye removal capacities and identifying environmentally friendly, low cost

and effective treatments is seen as environmentally and economically necessary. Most dye removal studies in the literature assess a treatments capacity to remove single dye-types. However, environmental dye contamination events are rarely in the form of single pure dyes and are often composed of mixtures of various dye types (i.e. azo, anthraquinone, reactive and acidic dyes).

Silicon dioxide (SiO_2) nanoparticles have gained increasing interest for several varying applications including catalysis, drug delivery, separation and bio-adsorption. As they possess a negative net charge due to Si-OH groups, surface functionalization is often required to enhance their ability to bind a range of differently charged entities e.g. anionic dyes [8]. Alkylsilane functionalization of oxide surfaces has recently been employed for binding nanoparticles to oxide surfaces and the attachment of organic ligands [9]. As alkylsilanes can self-assemble onto oxides, functional groups from these complexes are free to interact with biomolecules for bio-sensing [10], drug delivery [11], DNA separation [12] and oil/water separation applications [13]. 3-Aminopropyl-triethoxysilane (APTES) is one such alkylsilane which has shown both biocompatibility and readily undergoes hydrolysis in aqueous media. This indicates that its potential for environmental harm is minimal whilst the functionality of its hydrolysed form, in regards to its binding to organic ligands, seems promising [14, 15].

Helianthus annuus husk (commonly known as sunflower seed husk) is an unutilised material that remains following commercial sunflower seed extraction. It is therefore a cheap resource which may contain phytochemicals capable of providing nanoparticles with beneficial morphologies. It contains oleic acid and many other phytochemicals (i.e. reducing sugars), which have been shown to interact with silicon based materials to induce porosity and increase surface area [16-18].

Herein we synthesize positively charged APTES derived silane nanoparticles in the presence of *H. annuus* husk phytochemicals (P-silane-NP). The resulting porous silane nanoparticles were employed as adsorbents to remove concentrated mixtures of azo, anthraquinone, acid and basic dyes from solution.
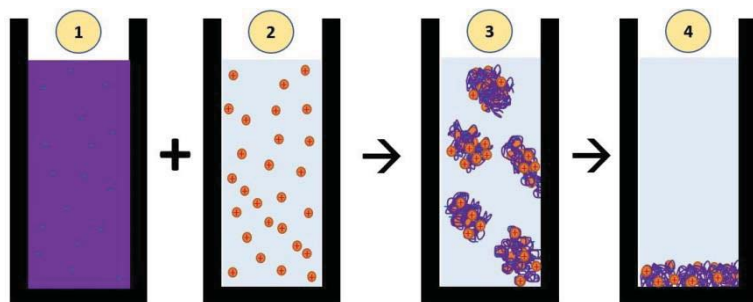
Scheme 1. Illustration of the concentrated dye removal process with positively charged silane nanoparticles. Negatively charged mixed dye solution (1) is mixed with positively charged soluble silane nanoparticles (2). The positive charge of the silane nanoparticles attracts the negatively charged dye and forms a complex which separates it from solution (3). The insoluble silane nanoparticle/dye complex settles and can later be removed (4).

2. Methods

2.1. Preparation of *H. annuus* Extract

Dried *H. annuus* husks (10 g) were added to 60 mL of ultrapure water (18 MΩ) and placed in a water bath at 90°C for 2 h and then allowed to cool at room temperature. The remaining solution was filtered through a 0.2 μm filter and stored at -20°C.

2.2. Synthesis of Silane Nanoparticles

Silane nanoparticles were prepared via hydrothermal method using APTES (Sigma-Aldrich, 99% purity). Briefly, 1 mL of APTES was added to 14 mL of ultrapure water (18 MΩ) or *H. annuus* husk extract prior to being subjected to hydrothermal treatment at 200°C for 2 h using a ramp up speed of 6.6°C per minute. The resulting water-soluble silane nanoparticles were filtered through a 0.2 μm syringe filter and subjected to dialysis for 48 h (MWCO 2000 Da). The dialysed solution was then

5

snap frozen using liquid nitrogen and lyophilised until desiccated. Un-functionalised silicon dioxide nanopowder (Sigma-Aldrich, 99.5% purity) with a particle size of 10-20 nm was used as a negative control.

2.3. Characterisation

2.3.1. Transmission Electron Microscopy (TEM)

Silane nanoparticles and SiO_2 nanoparticles were prepared by drop coating the samples on a holey-carbon grid. Morphological characteristics of the particles were visualised using a JEOL 1010 TEM operated at an accelerating voltage of 100 kV and JEOL 2010 at an accelerating voltage of 200 kV.

2.3.2. Scanning Electron Microscope Energy Dispersive X-ray Spectroscopy (SEM-EDS)

Elemental surface analysis of silane nanoparticles and SiO_2 nanoparticles was determined by subjecting them to EDS analysis using Oxford X-MaxN 20 EDXS Detector (2014) and AztecEnergy analysis software in conjunction with a Phillips XL30 SEM. Nanoparticles were lyophilised prior to use and were analysed as prepared.

2.3.3. X-ray photoelectron spectroscopy (XPS)

Chemical analysis of silane nanoparticles was performed using XPS (Thermo Scientific K-Alpha) with monochromated Al K-alpha source (1487.6 eV). Charge compensation using a flood gun was required. Peak fitting was performed using the Thermo Scientific Avantage XPS software package. The background signal subtraction of each core peak region of each sample was removed using a Shirley background model.

2.3.4. Fourier Transform Infrared Spectroscopy (FTIR)

FTIR spectra of lyophilised dye, silane nanoparticles and SiO$_2$ nanoparticles before and after remediation were determined by FTIR (Perkin Elmer Frontier). An average of 32 scans was collected for each measurement with a resolution of 4 cm^{-1} in the range of 4000–400 cm^{-1} using a percentage transmission spectrum.

2.3.5. X-ray Diffraction (XRD)

The crystallinity of silane nanoparticles and SiO$_2$ nanoparticles was determined by XRD using a Bruker AXS D8 Discover diffraction instrument equipped with a Cu-K alpha radiation source (wavelength 0.1542 nm) operating at 40 kV and 35 mA. All X-ray data was obtained in the θ −2u locked-couple mode over a 2θ interval of 10–90˚.

2.3.6. Zeta Potential

Particles charge dynamics were measured using a Malvern 2000 Zetasizer following appropriate dilution and sonication within a DTS 1060C, Malvern cuvette.

2.3.7. Brunauer–Emmett–Teller (BET) surface area measurements

Nitrogen adsorption-desorption isotherms were performed on a Micromeritics (ASAP 2400) analyser at -196 ^{o}C using liquid nitrogen (N$_2$). BET analysis was employed to determine the surface area of the samples by N$_2$ multilayer adsorption, measured as a function of relative pressure using a fully automated analyser. The pore characteristics of the synthesized samples were measured using the Barrett-Joyner-Halenda (BJH) formulae from N$_2$ isotherms. Prior to BET analysis, samples were degassed at 160 ^{o}C in a vacuum overnight.

2.4. Dye removal

Methyl Blue (dye content 82 %), Acid red 88 (dye content 75 %), Remazol brilliant blue R (dye content 50 %) and Acid green 25 dyes (dye content 75 %) (Sigma-Aldrich) were mixed together in an

equal concentration and a 1:1:1:1 (v/v) ratio (adjusted for percentage dye concentrations) to make a concentrated dye mixture of 1500 mg L^{-1}. These four dyes were chosen as they represent four different classes of dyes which are widely used in real-world textile processes.

Silane nanoparticle and SiO$_2$ nanoparticles were resuspended in phosphate buffered saline (PBS) (pH 7), warmed to 30˚C to solubilise particles and added to the dye at a final concentration of 5, 2.5, 1.25 and 0.63 g L^{-1}. After 5 min and 30 min, λ_{max} (OD$_{610}$) measurements were taken using a BMG CLARIOstar® spectrophotometer using Costar flat bottom 96 well plates.

Although the four individual dyes have different lambda max, when combined they form a complex that has one predominant peak at 610 nm. During mixed dye adsorption studies with silane treatments, all peaks and peak shoulders showed a decreased optical density relative to each other (S. Figure 1). It is recommended that when using this treatment for different dye types or different concentrations of the same dyes, absorbance spectral scans are used to identify dye removal efficiencies.

Mixed dye removal efficiency (%) was calculated as follows:

$$\text{Mixed dye removal efficiency (\%)} = 100 - ((C_t \div C_0) \times 100)$$

Where C_0 is the OD$_{610}$ of the mixed dye solution at time 0 and C_t is the OD$_{610}$ of mixed dye solution at time t.

The amount of dye adsorbed at equilibrium was determined from the following equation:

$$q_e = \frac{(C_0 - C_e).V}{W}$$

Where q_e is the adsorbents adsorption capacity (mg g^{-1}) at equilibrium, C_0 and C_e are the initial and final dye concentrations (mg L^{-1}), V is the volume of dye solution (L) and W is mass of adsorbent added (g).

2.5. LIVE/DEAD Baclight Bacterial Viability Assay

To visualize the viability of *E. coli* cells that were subjected to remediated supernatants from silane treatments, concentrated mixed dye solution (1500 mg L^{-1}) and APTES precursor, a LIVE/DEAD Baclight bacterial viability kit (L-7007, Invitrogen) was used as per manufacturer's instructions. Propidium iodide (red fluorescent dye) was used to label dead bacterial cells and SYTO 9 (green fluorescent dye) was used to label both live and dead microbial cells. The stained bacteria were transferred to a glass slide with cover-slip and were then observed using oil immersed 100x objective lens using a Leica DM2500 fluorescence microscope. Overlay images of red and green fluorescence were generated and cells showing red fluorescence were classified as dead and ones only showing green fluorescence corresponded to live cells.

2.6. Statistics

Univariate ANOVA pairwise comparison coupled with Tukey and Duncan *post hoc* tests were used to identify correlations at a 0.05 confidence interval.

3. Results:

3.1. TEM

APTES was utilised as a silicon source for the generation of silane nanoparticles (Figure 1 and S. Figures 2A & 2B) via hydrothermal treatment. APTES was added to either aqueous *H. annuus* husk plant extract or water and subjected to hydrothermal treatment for 2 h at 200°C to create porous silane nanoparticles (P-silane-NP) and silane nanoparticles (silane-NP) respectively. Both treatments were comprised of nanoparticles with some agglomeration characteristics when dried and imaged

9

via TEM (Figure 1A & B) with the silane-NP treatment showing an increased tendency to agglomerate. The P-silane-NP treatment possessed nanoparticle with sizes between 10-80 nm and the silane-NP treatment mostly possessed particles between 30-110 nm in size.

High resolution TEM images showed < 0.5 nm sized speckles present on the P-silane-NP nanoparticles which were absent in the silane treatment (S. Figures 2A & 2B respectively). These are likely to be disordered mesopores as suggested by Wei *et al*. 1998, or the formation of carbon quantum dots from the carbonaceous phytochemicals of the *H. annuus* extract during hydrothermal synthesis conditions [19]. This is reinforced by the increase in particles fluorescence seen in the P-silane-NP treatment (S. Figure 4 & 5).
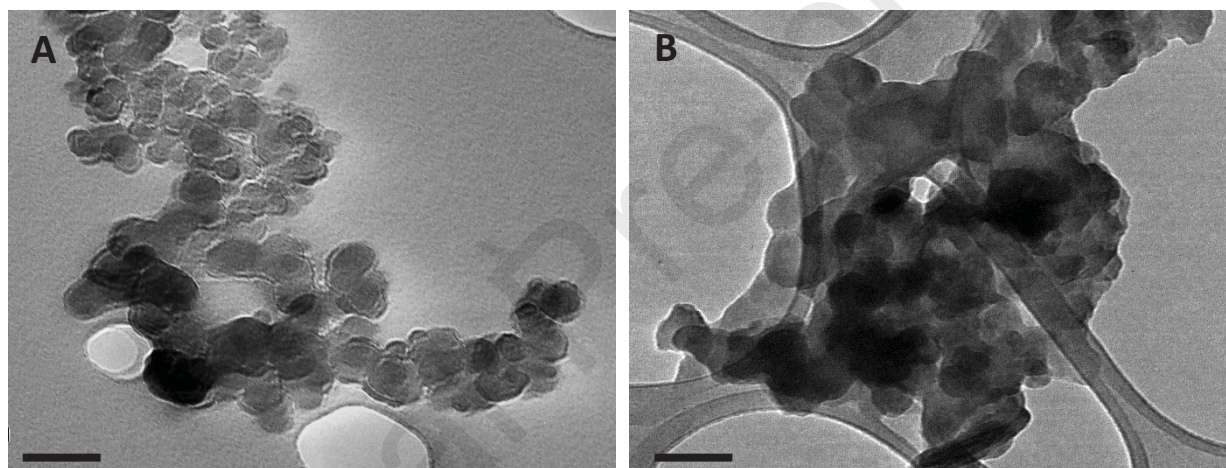
Figure 1: Representitive TEM images of (A) P-silane-NP and (B) silane-NP treatments. Scale bar represents 100 nm

3.2. XRD

P-silane-NP nanoparticles and SiO_2-NP's exhibited an amorphous nature with 27.3 and 30.1% crystallinity respectively (S. Figure 6). A comparison of the XRD fingerprint between samples shows only a slight increase in crystallinity with silane-NP nanoparticles over the P-silane-NP treatment. Conversion of amorphous silicon to crystalline silicon at 200°C is dependent on exposure time, with exposures less than 3 h producing minimal crystallinity [20, 21]. The lack of crystalline phases in the

P-silane-NP sample is likely due to carbon from the plant extract interfering with the silicon crystallisation process, essentially at temperatures lower than 230°C) [22-24].

3.3. EDS and XPS

Energy-dispersive X-ray spectroscopy spectra of both silane treatments showed that carbon, nitrogen, oxygen and silicon were present; however, nitrogen was absent in the SiO_2 treatment (S. figure 7). Energy-dispersive X-ray spectroscopy is often used as a surface analysis tool as its sample penetration depth is only 1-2 μm. However, quantitative measurements of light elements (i.e. carbon, oxygen and nitrogen) are inaccurate without comparison with standardised reference samples. X-ray photoelectron spectroscopy was therefore used to determine the atomic elemental percentage of the silane derived treatments.

X-ray photoelectron spectroscopy (XPS) analysis revealed a composition of 52.6% carbon, 30.4% oxygen, 4.1% nitrogen and 8.8% silicon in the P-silane-NP sample compared to 76.3% carbon, 18.3% oxygen, 1.6% nitrogen and 3.9% silicon in the silane-NP treatment (Table 1). It is interesting to note that even in the presence of carbonaceous phytochemicals from the *H. annuus* extract, the surface carbon of P-silane-NP is lower than that of the silane-NP treatment. Carbon within this sample is likely to act as a template for the silanes and be present under the functionalised layer. Templating of silanes, especially in the presence of elevated temperatures has been linked with more ordered Si-O-Si bonds bound to the template and increased -NH groups present at the interface of nanoparticles and solution phases [25]. This may explain the increased nitrogen content found at the surface of P-silane-NP (4.1%) compared to the silane-NP treatment (1.6%).

Table 1: XPS atomic elemental composition of the P-silane and silane nanoparticles surfaces

Sample	Atomic Percentage (at. %)				
	Carbon	Oxygen	Nitrogen	Silicon	Other
P-silane-NP	52.61	30.43	4.14	8.78	4.04

| Silane-NP | 76.32 | 18.26 | 1.56 | 3.86 | N/A |

XPS Interpretation of the nitrogen (1s) spectrum for P-silane-NP and silane-NP treatments was conducted to determine the nitrogen species present on the particles surface (Figure 2). P-silane-NP showed peaks at 398.8, 399.9 and 401.3 eV corresponding to pyridinic/amino nitrogen, NSi_2O/pyrrolic/amide nitrogen and graphitic/quaternary protonated nitrogen respectively [26-30]. silane-NP treatment possessed peaks at 398.9 eV corresponding to pyridinic/amino nitrogens and peaks 400.3 and 400.8 eV corresponding to NSi_2O/pyrrolic/amide nitrogen or nitrogen in pyridone functionalities [28, 30, 31]. Graphitic/quaternary protonated nitrogen was only present on the P-silane-NP treatment and is more positively charged than the pyridinic nitrogen found on the silane-NP treatment. This may account for the increased binding capacity of the P-silane-NP treatment to anionic dye species [30].

XPS analysis of carbon (1s) spectra showed little resolvable deviations between both silane treatments with C1s peaks located at 283.9 ± 0.1, 284.6 ± 0.1, 285.7 ± 0.2 and 288.2 ± 0.1 eV corresponding to sp2 carbon, C-C, C-O-C and to O-C=O functionalities respectively (Figure 2 and S. Table 3). Oxygen bonds present were also similar between samples (although in different relative abundances) showing O-Si-O species at ~532.9 eV, Si-O features at 530.7± 0.1 eV [32] and organic C-O between 531.4± 0.3 eV (Figure 2 and S. Table 3). Resolvable silicon peaks for P-silane-NP were found at 101.0, 101.7 and 102.2 eV corresponding to Si-O-C, Si in the form of Si_3N_4 and Si–O bonds [33, 34]. For the silane-NP treatment, the resolvable silicon peaks were found at 101.31, 102.02 and 102.73 eV corresponding to Si-C, Si–C and Si-Si bonds (Figure 2 and S. Table 3) [19, 35].

12
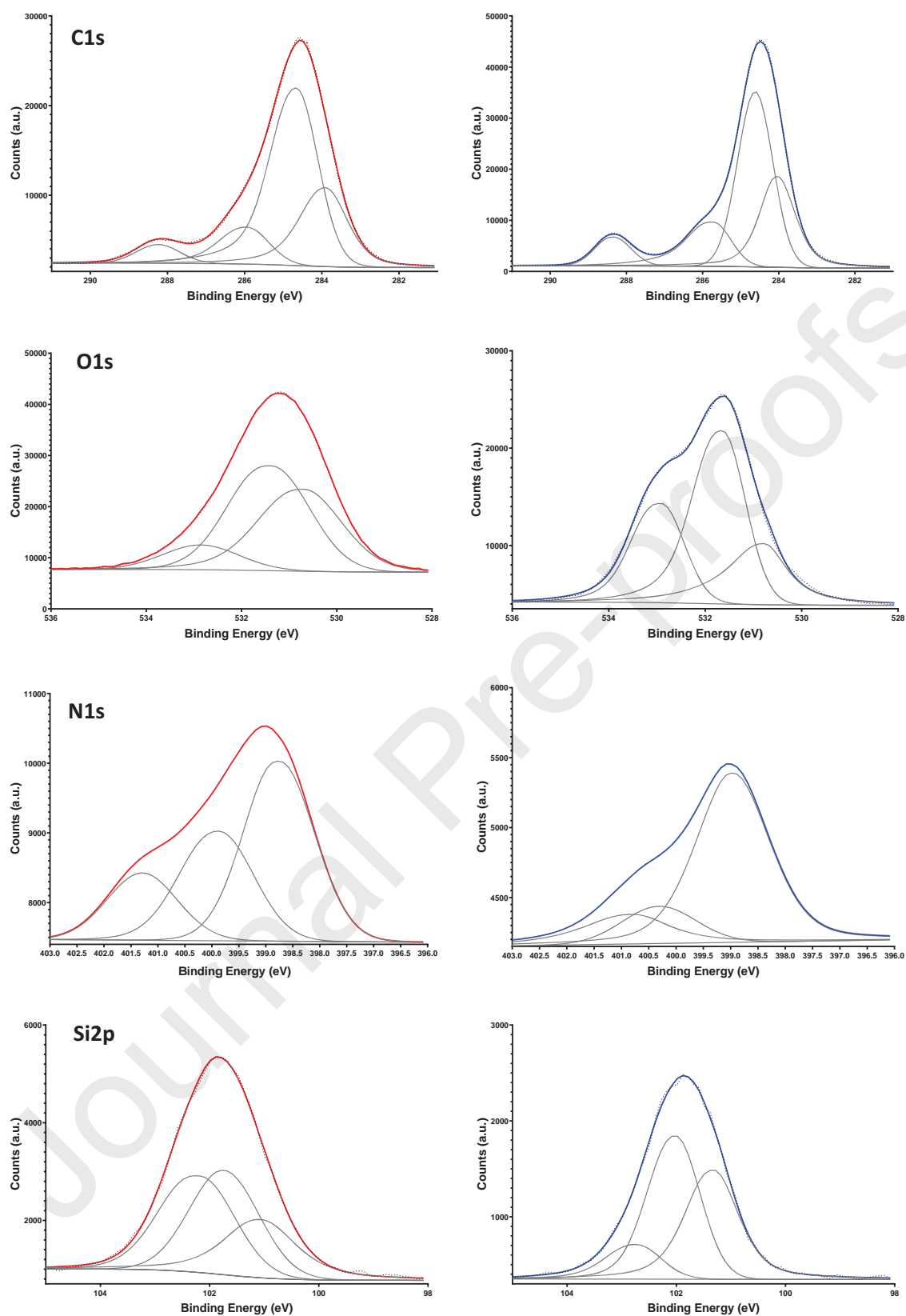
Figure 2: XPS spectra of P-silane-NP (red) and silane-NP (blue); high resolution core level spectra of carbon (C1s), oxygen (O1s), nitrogen (N1s) and silicon (Si2p) respectively

3.4. FTIR

Silicon dioxide has been shown to possess three distinct FTIR frequency regions, 1000-1100 cm^{-1} corresponding to Si-O-Si vibrations, 700-800 cm^{-1} corresponding to O-Si-O vibrations and 440-460 cm^{-1} corresponding to Si-O entities [9, 36, 37]. Considering the sample composition, the greater number of oxygen atoms bound to silicon atoms results in a shift in the peaks to a higher wavenumber. In this study, P-silane-NP showed peaks within this region at 1033, 748 and 442 cm^{-1} whilst silane-NP had peaks located at 1043, 776 and 442 cm^{-1} (Figure 3). SiO_2-NP without functionalization possessed peaks at 1076, 796 and 455 cm^{-1} (Figure 3). This indicates that all samples contained silicon dioxide moieties.

Although the source of silicon and nitrogen was derived from APTES, this precursor rapid hydrolyses in water. The absence of bands near 2975, 1104 and 1089 cm^{-1} indicate that the $Si-OC_2H_5$ group from APTES is absent and that it has been hydrolysed into silanetriols $((OH)_3Si(CH_2)_3NH_2)$ [38, 39].

Nitrogen groups responsible for providing a positive charge within the silicon-oxygen rich matrices of both silane treatments are located at 1558 and 1634 cm^{-1} confirming the presence of asymmetric -NH_3^+ (ammonium) deformations and -NH_2 bending groups respectively [9, 40] (Figure 3). These groups are responsible for adding a positive charge to the particles. This is supported by differences in zeta potentials between SiO_2 and silane particles (Table 4) and XPS analysis (Figure 2).

Bonds showing the attachment of carbon to silicon were visualised at 691 cm^{-1} confirming the presence of Si-CH_2 stretch/ Si-O-C moieties. Additional carbon bonds were visualised within both silane samples. The P-silane-NP treatments –CH_2 stretching modes were identified at 3046, 2933 and 2880 cm^{-1} frequencies (Figure 3). The presence of –CH stretching modes were also identified on silane-NP nanoparticles at 2973 2989, and 2903 cm^{-1} representing -CH_3 and –CH attachments respectively [41-43].

Specific carbonaceous bonds derived from the *H. annuus* husk extract were not obviously identifiable on the P-silane-NP treatment through FTIR analysis. The comparable XPS spectra for carbon (C1s) on the P-silane-NP and silane-NP treatments (Figure 2) indicates that phytochemicals from the *H. annuus* husk extract are likely not to coat the surface of the P-silane-NP treatment.
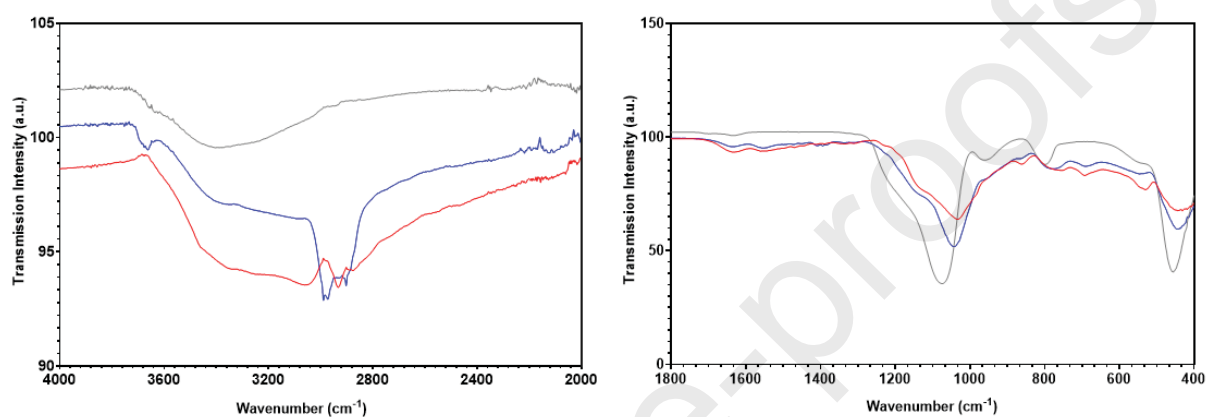
Figure 3: FTIR transmission profiles for P-silane-NP (red), silane-NP (blue) and SiO_2-NP's (grey) between (A) 4000 – 2000 cm^{-1} and (B) 1800- 400 cm^{-1})

3.5. BET Surface Area Analysis

Silane nanoparticle porosity and surface area was determined by subjecting the silane nanoparticles to BET analysis (Figure 4). In this analysis, the physical adsorption of N_2 gas molecules onto the surface of the silane particles was used to determine the materials specific surface area and pore size distribution. The N_2 absorption capacity of P-silane-NP show a typical type IV isotherm according to the IUPAC classification [44] indicating a mesoporous nature. A reduced N_2 adsorption profile with differing desorption characteristics (as seen by the absence of the hysteresis loop) was observed within the silane-NP treatment. This is representative of a type II isotherm indicating a non-porous or macroporous nature. A significant increase in surface area, indicated by an increased nitrogen absorption capacity was observed with the P-silane-NP (15.26 m^2 g^{-1}) compared to the nitrogen

15

absorption capacity of the silane-NP (4.88 m^2 g^{-1}) (S. Table 2). This is due to an increase in the number of pores and subsequent pore volume (0.0753 cm^3 g^{-1} and 0.0062 cm^3 g^{-1} respectively) of the P-silane-NP treatment compared to that of the silane-NP treatment. The measurement of pore diameters below 2 nm is inaccurate using nitrogen absorption BET analysis [45]; this may be why pore sizes of below 0.3 nm (as seen in the HR-TEM images in S. Figure 2A) may not have been identified in the Barrett–Joyner–Halenda (BJH) pore-size distribution curve (S. Figure 8). Findings from this analysis show that the influence of *H. annuus* husk extract during the synthesis of silane nanoparticles resulted in an increased porosity and surface area of the treatment when compared to those synthesized in water alone.
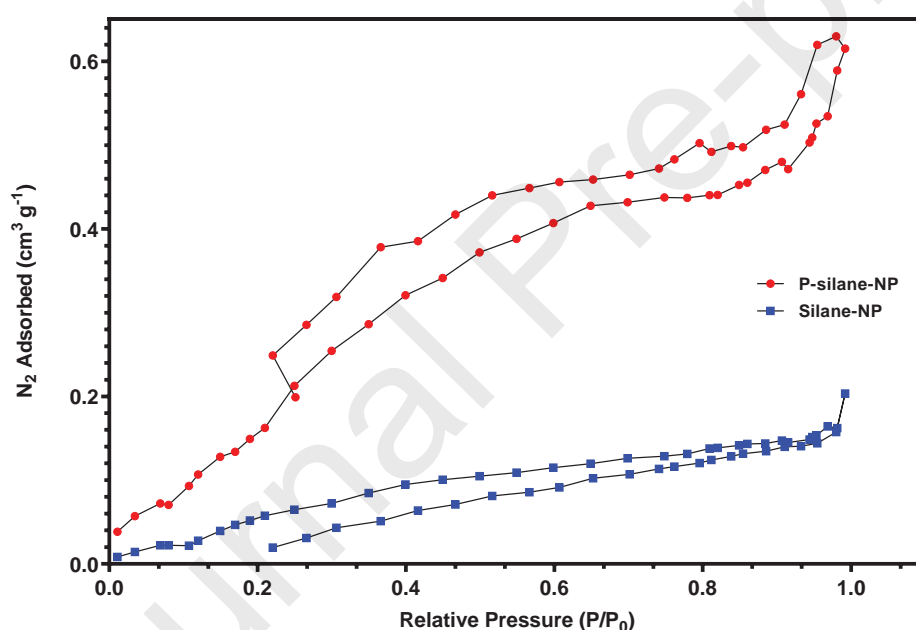
Figure 4: Nitrogen adsorption/desorption isotherms of P-silane-NP and silane-NP treatments

3.6. Mechanism of Increased Porosity

Helianthus annuus husk extract has been reported to contain approximately 4% protein, 5% lipid, 85% carbohydrate and 6% water [18, 46]. Antioxidant, phenolic, protein and lipid concentrations were low (S. Table 4 & 5) within the aqueous *H. annuus* husk extract and are therefore unlikely to

have significant interactions with the silanes. However, reducing sugars are reported to be a major water soluble component of *H. annuus* husk with an approximate total biomass concentration of 26% [47].

Reducing sugar concentrations of our extract were determined via the DNS assay and found to be at 1.49 mg mL^{-1} glucose equivalents (S. Table 5). When considering the total volume of *H. annuus* husk extract and silicon precursor (APTES) in the reaction vessel for the P-silane-NP treatment, the concentration of reducing sugars was 2% (mg L^{-1}) of the silane concentration present. This is supported by FTIR analysis of the *H. annuus* extract which shows the presence of bonds at 1143 and 970 cm^{-1} which are representative of stretching vibrations of the C-O-C within the glycosidic bridge (β-glycosidic bonds) and an α-glycosidic bond at 837 cm^{-1} which are all characteristic of sugars [48, 49] (S. figure 9).

Wei et al., (1998) showed that the use of reducing sugars (D-glucose and D-maltose) were able to act as templates for generating mesoporous silica with large surface area, large pore volumes and narrow pore size distributions [16]. The morphology of these silica particles and their disordered mesopores are comparable to findings from this study (S. Figure 2A).

The mechanism underlying increased silane porosity in the presence of *H. annuus* husk extract can be explained by the interaction and binding of the carbohydrate derived phytochemicals (i.e. reducing sugars) with the silane which create cavities in its surface. Following hydrothermal treatment, interactions between these compounds and the silane nanoparticles become weak and dislodge from the silane. However, the cavities they have created in the surface remain, increasing porosity [50-54]. This phenomenon has been demonstrated with surfactants i.e. (polystyrene-b-poly(acrylic acid) (PS-b-PAA) and CTAB as co-templates [55] and organic non-fatty compounds i.e. reducing sugars [16, 17].

3.7. Concentrated Dye Removal

17

Adsorption is currently the most utilised dye remediation strategy as it is rapid and environmentally friendly. Adsorption approaches for dye removal treatment do not degrade the original dye molecule, preventing release of toxic break-down intermediates [7]. Activated carbon is a commercial dye adsorbent with removal rates of between 14.7 - 603.3 mg g^{-1}. Its efficiency as an adsorbent depends on the biological source of the carbon, surface area of the particles and the type of dye it is employed to remove [56-58]. Silicon nanoparticles have been hailed for their potential use as adsorbents due to their biocompatibility and tuneable surface areas, however, un-functionalised silicon nanoparticles possess a negative charge which prevents the adsorption of anionic pollutants. Functionalization of these nanoparticles with positively charged functional groups is therefore required for sufficient binding of anionic dyes.

To determine if our positively charged silane nanoparticles were able to adsorb dye via a monolayer or stacking phenomenon, Langmuir and Freundlich isotherms were applied to our data.

Langmuir isotherms were generated by plotting $C_e \div q_e$ vs C_e where $q_{max} = 1 \div$ slope and $b =$ slope $\div$ intercept. The Langmuir equation can be expressed linearly as;

$$\frac{C_e}{q_e} = \frac{1}{b.\, q_{max}} + \frac{C_e}{q_{max}}$$

Where C_e is the equilibrium dye concentration (mg L^{-1}), q_e is the amount of dye adsorbed at equilibrium (mg g^{-1}), q_{max} is the maximum adsorption capacity (mg g^{-1}) and b is the Langmuir constant.

The feasibility of absorption was determined by the separation factor (R_L) which is dimensionless and can be expressed as:

$$R_L = \frac{1}{(b.\, C_0) + 1}$$

Where R_L is dimensionless, C_0 is the initial dye concentration (mg L^{-1}) and b is the Langmuir constants.

Freundlich adsorption capacities were determined by plotting $Log\ q_e\ vs\ Log\ C_e$ and applying this data to the following equation:

$$q_e = K_F . C_e^{1/n}$$

Where q_e is the amount of dye adsorbed at equilibrium (mg g^{-1}), C_e is the equilibrium dye concentration (mg L^{-1}), $1/n$ is the slope of the line and K_F is the Freundlich constant.

The results from this study show a calculated dye removal capacity of 731.04 and 454.96 mg g^{-1} for P-silane-NP and silane-NP treatments respectively, based on the average dye removal capacity of the unsaturated treatments (area of the graph which had not plateaued) at 1.25 g L^{-1} dosage (Table 3 & Figure 5). This is in good agreement with their corresponding Langmuir isotherm adsorption capacity extrapolations of 714.29 and 416.67 mg g^{-1} respectively. The R^2 values for the Langmuir isotherms for both treatments were between 0.96-0.99 which supersede that of the Freundlich model with R^2 values between 0.73-0.77 (Table 3). It is therefore anticipated that the adsorption process proceeds via a monolayer adsorption route where dye molecules bind to vacant sites on the adsorbent and do not stack on top of each other in multiple layers [59-61].

The feasibility of adsorption was determined by the separation factor (R_L) where; $R_L > 1$ indicates desorption, $R_L = 0$ shows a very strong binding affinity, $R_L > 0$ but < 1 indicates a favourable adsorption and $R_L = 1$ relates to a linear adsorption [40, 62]. P-silane-NP and silane-NP possessed R_L parameters of 1.4×10^{-6} 2.4×10^{-6} representing a very strong binding affinity.

To date, *in vitro* studies of dye removal with functionalised silica nanoparticles have predominantly focused on single dye types and if mixtures have been used, their concentrations are often low (Table 2) [63-66]. This is not representative of real-world textile waste contamination events where

19

concentrated dye mixtures i.e. blends of azo, anthraquinone, acid, basic and reactive dyes, are blended together and released into the environment [67-69]. In fact, to the best of our knowledge, our P-silane-NP treatment shows the highest reported concentrated mixed dye removal efficiency when compared to other silicon derived treatment approaches. Comparison of our treatment with other recently published adsorbents is demonstrated in table 2.

Table 2: Comparison of the adsorption capacities of different dyes on various adsorbents from recently published works

Adsorbent	Dye type	pH of dye	Volume of dye (mL)	Initial dye concentration (mg L^{-1})	Adsorbent dosage (mg L^{-1})	Adsorption efficiency (mg g^{-1})	Reference
Silane Nanoparticles synthesized with H. annuus extract (P-silane-NP)	Cocktail of Methyl Blue, Acid red 88, Remazol brilliant blue R and Acid Green 25	5.8	5	1500	1250	714.29	This work
Silane Nanoparticles (silane-NP)	Cocktail of Methyl Blue, Acid red 88, Remazol brilliant blue R and Acid Green 25	5.8	5	1500	1250	416.67	This work
Metal organic framework (UiO-66)	Methyl Orange	5.9	50	20	200	84.8	[70]
Nano-silica fabricated with silver nanoparticles	Cocktail of Congo Red, Eosin Yellow, Bromophenol Blue, Brilliant Blue (BB)	4.2, 6.8, & 9.1	25	50	2000	547.5	[71]
Graphene oxide–chitosan nanocomposite	Cocktail of Acid Yellow & Acid Blue 74	2-10	NA	22	600	85.7	[72]
ZnS-activated carbon composite	Brilliant Green	5	50	7	30	258.70	[73]
Cubic mesoporous silica SBA-16 with carboxylic acid	Methylene Blue	9	NA	500	<250	561	[74]
Mixed silica–alumina oxide	Direct Blue 71	5.3-6.4	20	30	1000	49.2	[75]
Methylimidazolium ionic-liquid-functionalized graphene oxide	Direct Red 80	2	100	50	400	501.3	[76]

20

(mimGO) sponge							
Highly porous, ultralight graphene oxide foam	Rhodamine B	3	30	50	300	446	[77]
magnetic amine/Fe_3O_4 functionalized biopolymer resin	Methyl Orange	5.5	100	200	1000	222.2	[78]
Mesoporous SiO_2 nanoparticles (MSN) decorated with SnO_2 quantum dots (QDs)	Methylene Blue	6.1	80	10	625	73.15	[79]

Dye removal curves for P-silane-NP (Figure 5) show saturated removal efficiency at 2.5 and 5 g L^{-1} with no statistical difference (one-way ANOVA coupled with Tukey and Duncan post-hoc tests). It was therefore important to extrapolate the dye removal efficiency at the lower concentration of 1.25 g L^{-1}. After 30 min 91.37% of the 1500 mg L^{-1} dye solution had been removed from solution with the treatment dosage of 1.25 g L^{-1}. The value for the silane-NP and SiO_2-NP treatments was 56.87% and 15.06% removal respectively for the same adsorbent dosage. Non-functionalised SiO_2 nanoparticles showed a maximum dye adsorption capacity of 41.25% with 5 g L^{-1} adsorbent. This supports the principle that negatively charged SiO_2 particles require functionalization with positive functional groups for sufficient anionic dye removal efficiencies. Visual representation of dye being drawn out of solution using the P-silane-NP treatment can be seen in S. Figure 10 and is represented graphically in Scheme 1.
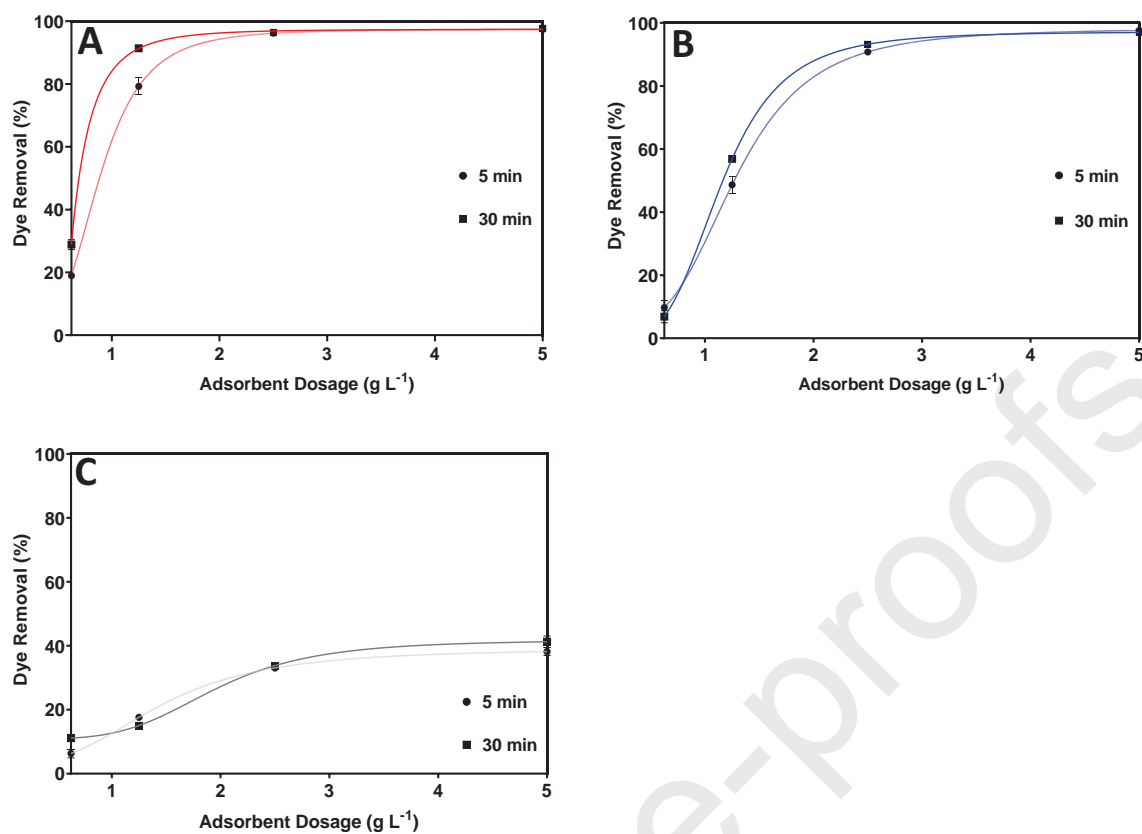
Figure 5: Removal of concentrated mixed dye solutions with different adsorbent dosages following 5 min and 30 min of exposure to (A) P-silane-NP (B) silane-NP and (C) SiO$_2$-NP

3.8. Langmuir and Freundlich isotherms

Table 3: Langmuir and Freundlich Parameters for the adsorption of concentrated mixed dyes using P-silane-NP and silane-NP

	P-silane-NP			Silane-NP	
Isotherm	Parameter	Concentrated dye (1500 mg L^{-1})	Isotherm	Parameter	Concentrated dye (1500 mg L^{-1})
Langmuir	q_{max} (mg g^{-1})	714.29	Langmuir	q_{max} (mg g^{-1})	416.67
	b (mg L^{-1})	11.31		b (mg L^{-1})	15.31
	R_L	1.40^{E-06}		R_L	2.40^{E-06}
	R^2	0.96		R^2	0.99
	Calculated q_{max} (mg g^{-1})	731.04		Calculated q_{max} (mg g^{-1})	454.96
Freundlich			Freundlich		

K_F (mg g^{-1})	60.46		K_F (mg g^{-1})	137.45
$1/n$	0.41		$1/n$	0.25
R^2	0.73		R^2	0.77

3.9. Zeta Potential

The zeta potential of un-functionalised SiO$_2$ nanoparticles has been shown to be moderately negative [80-82] which is consistent with our findings (-17.57 mV). Both P-silane-NP and silane-NP treatments contain SiO$_2$ bonds as can be seen in the FTIR spectra; however, they possess positive charges with zeta potentials between 13.22-8.20 mV respectively (Table 4). The reverse in charged state can be explained by the presence of electronegative pyridinic/amino, pyrrolic/amide, graphitic/ quaternary nitrogen groups within the silica matrix [83-87]. The strong binding affinity between the silane treatments and the dye is due to electrostatic attraction between the negatively charged dye molecules and the positively charged electronegative nitrogen groups on the silane treatments [86-88].

Aggregation of particles is dependent on the number of collisions between particles and the attachment of colliding particles. Systems possessing high colloidal stability possess a low collision frequency due to repulsive charges between particles [89]. In this system, the addition of the silane nanoparticles to the dye has resulted in both particle collisions and complex formation between silanes and dye molecules resulting in aggregation and flocculation. The increased nitrogen content found on the P-silane-NP compared to silane-NP sample has been shown in the XPS analysis (4.14 and 1.56 at. % respectively). This was reinforced by zeta potential measurements (Table 4) where the P-silane-NP treatment possessed an increased positive charge over the silane-NP treatment (13.22 and 8.20 mV respectively). The increase in positive charge of the P-silane-NP compared to that of the silane-NP treatment and the treatments larger surface area are associated with its increased capacity for dye adsorption.

Table 4: Zeta potential measurements of adsorbent treatments and dye at pH 7

Treatment	Zeta Potential (mV)
P-silane-NP	13.22 (SE 0.14)
Silane -NP	8.20 (SE 0.30)
SiO$_2$-NP	-17.57 (SE 0.37)
Dye	-54.23 (SE 1.06)

3.10. Mechanism of Concentrated Dye Removal

Silane nanoparticles synthesized in the presence of phytochemicals from *H. annuus* showed significantly higher surface area than those synthesized in water alone with nitrogen absorption capacities of 15.26 and 4.88 m^2 g^{-1} respectively (Figure 4). Increased surface area allows for more reactions and interactions with dye molecules at the particles surface. This coupled with increased dye binding functionalities of the P-silane-NP surface compared to that of silane-NP, which was supported by the treatments increased nitrogen content determined from XPS (Table 1), further increases dye binding capacity.

P-silane-NP's were shown to contain more nitrogen containing groups on their surface when compared to the silane-NP treatment (4.14 and 1.56 AT% respectively) via XPS analysis (Table 1). The presence of carbonaceous materials from the *H. annuus* extract is likely to provide an anchor for the APTES to bind and condense following heat treatment leading to more ordered structures with nitrogen groups facing out from the particles surface when compared to silanes without a template [25, 90, 91].

Silane nanoparticle treatments that were added to concentrated dye mixtures in powdered form showed significantly reduced dye removal capacity (~50%) when compared silanes which have been solubilised in water prior to dye adsorption (S. Figure 12). Soluble silane particles bind to the negatively charged dye molecules with their electronegative nitrogen groups which results in

24

interfacial separation of the dye-silane complex from solution. Colloidal stability of the aqueous silanes is interrupted once the dye is bound due to the formation of a dye-silane complex. This phenomenon causes aggregation and results in altered charge characteristics of the treatment. The result is a collapse of the electric double layer preventing the particles possessing the required activation energy required to remain in solution [92].

Although the silane nanoparticles both showed positive charges, their charged state was quite low indicating incipient instability in solution (Table 4). Particles with zeta potentials between 0 – ±5 mV rapidly coagulate and flocculate out of solution, particles showing moderate aqueous stability possess potentials between ±30- ±40 mV and good colloidal stability is achieved over 40 mV. Within the described system, negatively charged dye binds to the weakly stable positively charged silane particles (13.22-8.20 mV) upsetting their colloidal stability resulting in their rapid coagulation and flocculation along with their bound dye molecules.

3.11. Bacterial viability

A key factor for any environmental remediation is whether the treatment itself poses any environmental harm. A number of metal nanoparticles and carbon nanotubes have been shown to induce microbial and mammalian toxicity [93]. Any chemical treatment may be hazardous and pose an environmental threat themselves [94].

Within this study treated concentrated dye solutions were assessed for their ecotoxicity against *E. coli* via a live/dead fluorescence staining assay. *E. coli* was used as an environmental toxicity indicator within this study as its presence in the environment is well documented and it can survive for prolonged periods in environmental conditions [95].

Within this study the *E. coli* was added to the supernatants from treatments which were spiked with silane nanoparticles for 4 hours. The bacteria were then subjected to a live/dead fluorescent stain to determine the toxicity of the treatment. Cell membranes that are intact and healthy uptake the green stain and damaged/dead cells result in the uptake of the red dye.

Supernatants from P-silane-NP and silane-NP treatments showed little toxicity towards *E. coli* with 90.1 and 83.1% bacterial viability respectively following a 4-hr exposure (Figure 6, images 1 and 2). Hydrothermal treatment of APTES and the removal of impurities via dialysis is likely to decrease the particles toxicity as microbial cultures subjected to APTES alone showed significant bacterial toxicity (15.1 % bacterial viability).

E. coli that was subjected to the concentrated dye mixture without any treatment was heavily damaged with its population only possessing 19.5 % viable cells. As expected, no significant toxicity was noticed in the sterile water control (Figure 6, images 3 and 5 respectively).
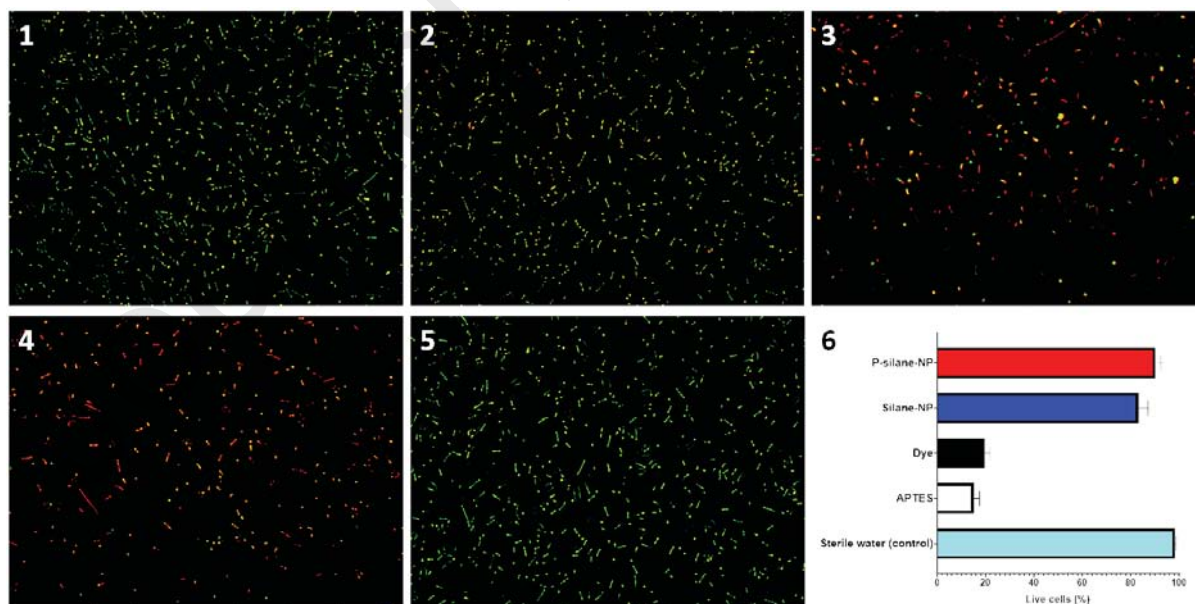
Figure 6: Environmental suitability of treatments using a fluorescence staining assay to determine live (green) and dead (red) *E. coli* 0157.H+ cells following a 4 hr incubation with; (1) P-silane-NP

treated supernatant (2) silane-NP treated supernatant (3) Concentrated dye mixture (1500 mg L^{-1})

(4) APTES (5mg L^{-1}) (5) sterile water Control. The percentage of live cells is represented in (6).

4.0. Conclusions

Functionalization of SiO$_2$ nanoparticles with alkylsilanes has been suggested as the basis for several technologies due to their inherent affinity for binding biomolecules and heavy metal ions. This study utilised APTES as a silicon and amine precursor for the generation of positively charged silane nanoparticles for concentrated dye removal from aqueous solutions. The addition of *H. annuus* husk extract to the synthesis solution resulted in an increased porous silane nanoparticulate assembly which led to amplified dye removal capacity when compared to silane nanoparticles alone. In addition, dye adsorption treatments synthesized in the presence of the extract possessed increased positive charges and elevated nitrogen concentrations on their surface (aiding dye adsorption). *H. annuus* husk extract itself did not contribute to the dye degradation, but its influence on the silanes resulted in nanoparticles with enhanced dye adsorption capacities.

Both bare silane nanoparticles and *H. annuus* husk infused silane nanoparticles showed 4-6 times increased dye removal capacity respectively when compared to that of SiO$_2$ nanoparticles at a concentration of 1.25 g L^{-1} and in the presence of 1500 mg L^{-1} mixed dye solution. The findings were substantiated by TEM, FTIR, SEM-EDS, XPS and zeta potential analyses. The silane dye removal strategy is one of monolayer adsorption affinity with Langmuir isotherms closely resembling the calculated adsorption capacity for 1.25 g/ L adsorbent dosage. The strong binding affinity was supported by R_L values of between 1.4×10^{-6} 2.4×10^{-6}. The high binding affinity of the dye to adsorbent can be explained by the electrostatic attraction between positively charged electronegative nitrogen groups from the silane nanoparticles and the negatively charged concentrated dye mixture. Enhanced dye removal from P-silane-NP's has been attributed to increase

27

dye-particle interactions due to increased particle porosity and surface area, increased number of positively charged functional groups on the surface of P-silane-NP's compared to other treatments and interfacial separation of unstable colloidal silanes from solution following binding dye. The environmental suitability of these particles is supported as the bacterial toxicity of remediated dye solutions using these particles was shown to be minor whilst the dye itself was damaging to *E. coli* cells. The use of waste plant material utilises an otherwise discarded material and in turn, lowers the cost of nanoparticle production which would traditionally require chemical modifications. The results from this study show a promising textile dye treatment technology with significant dye adsorption capacity and minimal potential for environmental harm. Future research should be directed towards treatment reusability following the desorption of dyes and the use of different waste materials to enhance silane nanoparticle properties for the removal of various anionic pollutants.

References

[1] M. Bilal, M. Asgher, R. Parra-Saldivar, H. Hu, W. Wang, X. Zhang, H.M.N. Iqbal, Immobilized ligninolytic enzymes: An innovative and environmental responsive technology to tackle dye-based industrial pollutants – A review, Sci. Total Environ. 576 (2017) 646-659.

[2] A. Truskewycz, R. Shukla, A.S. Ball, Phytofabrication of Iron Nanoparticles for Hexavalent Chromium Remediation, ACS Omega 3(9) (2018) 10781-10790.

[3] K. Velayutham, A.K. Madhava, M. Pushparaj, A. Thanarasu, T. Devaraj, K. Periyasamy, S. Subramanian, Biodegradation of Remazol Brilliant Blue R using isolated bacterial culture (Staphylococcus sp. K2204), Environ. Technol. (2017) 1-8.

[4] K.Z. Elwakeel, A.A. El-Bindary, A. Ismail, A.M. Morshidy, Magnetic chitosan grafted with polymerized thiourea for remazol brilliant blue R recovery: Effects of uptake conditions, Journal of Dispersion Science and Technology 38(7) (2017) 943-952.

[5] D. Bhatia, N.R. Sharma, J. Singh, R.S. Kanwar, Biological methods for textile dye removal from wastewater: A review, Critical Reviews in Environmental Science and Technology 47(19) (2017) 1836-1876.

[6] L. Chen, L. Wang, X. Wu, X. Ding, A process-level water conservation and pollution control performance evaluation tool of cleaner production technology in textile industry, Journal of Cleaner Production 143 (2017) 1137-1143.

[7] F. Chen, E. Zhao, T. Kim, J. Wang, G. Hableel, P.J.T. Reardon, S.J. Ananthakrishna, T. Wang, S. Arconada-Alvarez, J.C. Knowles, J.V. Jokerst, Organosilica Nanoparticles with an Intrinsic Secondary Amine: An Efficient and Reusable Adsorbent for Dyes, ACS Applied Materials & Interfaces 9(18) (2017) 15566-15576.

[8] S. Pal, A.S. Patra, S. Ghorai, A.K. Sarkar, V. Mahato, S. Sarkar, R.P. Singh, Efficient and rapid adsorption characteristics of templating modified guar gum and silica nanocomposite toward removal of toxic reactive blue and Congo red dyes, Bioresour. Technol. 191 (2015) 291-299.

[9] D. Meroni, L. Lo Presti, G. Di Liberto, M. Ceotto, R.G. Acres, K.C. Prince, R. Bellani, G. Soliveri, S. Ardizzone, A Close Look at the Structure of the TiO2-APTES Interface in Hybrid Nanomaterials and Its Degradation Pathway: An Experimental and Theoretical Study, The Journal of Physical Chemistry C 121(1) (2017) 430-440.

[10] H. Manisha, P.D. Priya Shwetha, K.S. Prasad, Low-cost Paper Analytical Devices for Environmental and Biomedical Sensing Applications, in: S. Bhattacharya, A.K. Agarwal, N. Chanda, A. Pandey, A.K. Sen (Eds.), Environmental, Chemical and Medical Sensors, Springer Singapore, Singapore, 2018, pp. 315-341.

[11] Y.-Y. Song, H. Hildebrand, P. Schmuki, Photoinduced release of active proteins from TiO2 surfaces, Electrochemistry Communications 11(7) (2009) 1429-1433.

[12] T. Nakazumi, Y. Hara, Influence of thickness of alkyl-silane coupling agent coating on separation of small DNA fragments in capillary gel electrophoresis, IOP Conference Series: Materials Science and Engineering 242(1) (2017) 012034.

[13] P. Seeharaj, P. Pasupong, E. Detsri, P. Damrongsak, Superhydrophobilization of SiO2 surface with two alkylsilanes for an application in oil/water separation, Journal of Materials Science 53(7) (2018) 4828-4839.

[14] S. Chandra, G. Beaune, N. Shirahata, F.M. Winnik, A one-pot synthesis of water soluble highly fluorescent silica nanoparticles, Journal of Materials Chemistry B 5(7) (2017) 1363-1370.

[15] L. Zhiting, D. Xuezhi, Q. Gang, Z. Xinggui, Y. Weikang, Eco-friendly one-pot synthesis of highly dispersible functionalized graphene nanosheets with free amino groups, Nanotechnology 24(4) (2013) 045609.

[16] Y. Wei, D. Jin, T. Ding, W.-H. Shih, X. Liu, S.Z.D. Cheng, Q. Fu, A Non-surfactant Templating Route to Mesoporous Silica Materials, Advanced Materials 10(4) (1999) 313-316.

29

[17] S. Das, D. Berke-Schlessel, H.-F. Ji, J. McDonough, Y. Wei, Enzymatic hydrolysis of biomass with recyclable use of cellobiase enzyme immobilized in sol–gel routed mesoporous silica, Journal of Molecular Catalysis B: Enzymatic 70(1) (2011) 49-54.

[18] S. Chandraju, R. Venkatesh, C.S.C. Kumar, B.A. Kumar, Estimation of Reducing Sugar by Acid Hydrolysis of Sunflower (<i>Helianthus annuus</i>) Husk by Standard Methods, Agricultural Sciences Vol.07No.05 (2016) 4.

[19] Z. Wang, P. Li, Y. Chen, J. Liu, W. Zhang, Z. Guo, M. Dong, Y. Li, Synthesis, characterization and electrical properties of silicon-doped graphene films, Journal of Materials Chemistry C 3(24) (2015) 6301-6306.

[20] S. Askari, R. Halladj, M. Sohrabi, An overview of the effects of crystallization time, template and silicon sources on hydrothermal synthesis of sapo-34 molecular sieve with small crystals, 2012.

[21] P. Bettermann, F. Liebau, The transformation of amorphous silica to crystalline silica under hydrothermal conditions, Contributions to Mineralogy and Petrology 53(1) (1975) 25-36.

[22] R.R. Devarapalli, S. Szunerits, Y. Coffinier, M.V. Shelke, R. Boukherroub, Glucose-Derived Porous Carbon-Coated Silicon Nanowires as Efficient Electrodes for Aqueous Micro-Supercapacitors, ACS Applied Materials & Interfaces 8(7) (2016) 4298-4302.

[23] M.M. Tang, R. Bacon, Carbonization of cellulose fibers—I. Low temperature pyrolysis, Carbon 2(3) (1964) 211-220.

[24] A.R.M. Dalod, L. Henriksen, T. Grande, M.-A. Einarsrud, Functionalized TiO(2) nanoparticles by single-step hydrothermal synthesis: the role of the silane coupling agents, Beilstein Journal of Nanotechnology 8 (2017) 304-312.

[25] S.K. Vashist, E. Lam, S. Hrapovic, K.B. Male, J.H.T. Luong, Immobilization of Antibodies and Enzymes on 3-Aminopropyltriethoxysilane-Functionalized Bioanalytical Platforms for Biosensors and Diagnostics, Chem. Rev. 114(21) (2014) 11083-11130.

[26] S.R. Kelemen, M. Afeworki, M.L. Gorbaty, P.J. Kwiatek, M.S. Solum, J.Z. Hu, R.J. Pugmire, XPS and 15N NMR Study of Nitrogen Forms in Carbonaceous Solids, Energy Fuels 16(6) (2002) 1507-1515.

[27] T. Susi, T. Pichler, P. Ayala, X-ray photoelectron spectroscopy of graphitic carbon nanomaterials doped with heteroatoms, Beilstein journal of nanotechnology 6 (2015) 177-192.

[28] E.N. Nxumalo, N.J. Coville, Nitrogen Doped Carbon Nanotubes from Organometallic Compounds: A Review, Materials 3(3) (2010).

[29] S. Maldonado, K.J. Stevenson, Influence of Nitrogen Doping on Oxygen Reduction Electrocatalysis at Carbon Nanofiber Electrodes, The Journal of Physical Chemistry B 109(10) (2005) 4707-4716.

[30] C. Domínguez, F.J. Pérez-Alonso, J.L. Gómez de la Fuente, S.A. Al-Thabaiti, S.N. Basahel, A.O. Alyoubi, A.A. Alshehri, M.A. Peña, S. Rojas, Influence of the electrolyte for the oxygen reduction reaction with Fe/N/C and Fe/N/CNT electrocatalysts, Journal of Power Sources 271 (2014) 87-96.

[31] X. Han, H. Chen, X. Li, J. Wang, C. Li, S. Chen, Y. Yang, Interfacial nitrogen stabilizes carbon-coated mesoporous silicon particle anodes, Journal of Materials Chemistry A 4(2) (2016) 434-442.

[32] S. Nsanzamahoro, F.P. Mutuyimana, Y. Han, S. Ma, M. Na, J. Liu, Y. Ma, C. Ren, H. Chen, X. Chen, Highly selective and sensitive detection of catechol by one step synthesized highly fluorescent and water-soluble silicon nanoparticles, Sensors and Actuators B: Chemical 281 (2019) 849-856.

[33] J. Schofield, S.C. Reiff, S.M. Pimblott, J.A. LaVerne, Radiolytic hydrogen generation at silicon carbide–water interfaces, Journal of Nuclear Materials 469 (2016) 43-50.

[34] X. Ma, D. Xu, P. Ji, C. Jin, J. Lin, Y. Ding, C. Xu, High-rate, room-temperature synthesis of amorphous silicon carbide films from organo-silicon in high-density helicon wave plasma, Vacuum 164 (2019) 355-360.

[35] J. Tung, L.S. Tew, C. Coluccini, Y.-D. Lin, Y.L. Khung, Grafting Behavior for the Resonating Variants of Ethynylaniline on Hydrogenated Silicon (100) Surfaces under Thermal Hydrosilylation, Chemistry – A European Journal 24(50) (2018) 13270-13277.

[36] M. Li, Z. Wu, J. Tan, Properties of form-stable paraffin/silicon dioxide/expanded graphite phase change composites prepared by sol–gel method, Applied Energy 92 (2012) 456-461.

[37] G. Fang, H. Li, X. Liu, Preparation and properties of lauric acid/silicon dioxide composites as form-stable phase change materials for thermal energy storage, Mater. Chem. Phys. 122(2) (2010) 533-536.

[38] A.L. Mohamed, M.A. El-Sheikh, A.I. Waly, Enhancement of flame retardancy and water repellency properties of cotton fabrics using silanol based nano composites, Carbohydrate Polymers 102 (2014) 727-737.

[39] C. Sun, Y. Zhang, C. Ruan, C. Yin, X. Wang, Y. Wang, W.W. Yu, Efficient and Stable White LEDs with Silica-Coated Inorganic Perovskite Quantum Dots, Advanced Materials 28(45) (2016) 10088-10094.

[40] S. Nayab, A. Farrukh, Z. Oluz, E. Tuncel, S.R. Tariq, H.u. Rahman, K. Kirchhoff, H. Duran, B. Yameen, Design and Fabrication of Branched Polyamine Functionalized Mesoporous Silica: An Efficient Absorbent for Water Remediation, ACS Applied Materials & Interfaces 6(6) (2014) 4408-4417.

[41] Z.-B. Zhao, L. Tai, D.-M. Zhang, Z.-F. Wang, Y. Jiang, Preparation of poly (octadecyl methacrylate)/silica-(3-methacryloxypropyl trimethoxysilane)/silica multi-layer core-shell nanocomposite with thermostable hydrophobicity and good viscosity break property, Chemical Engineering Journal 307 (2017) 891-896.

[42] M.A. Abarghooei, R. Mohebat, Z. Karimi-Jaberi, M.H. Mosslemin, Nano-silica supported palladium nanoparticles: A sustainable nanocatalyst for efficient synthesis of 2,3-diarylimidazo[1,2-a]pyridines at low catalyst loading, Catalysis Communications 105 (2018) 59-64.

[43] V. Ţucureanu, A. Matei, A.M. Avram, FTIR Spectroscopy for Carbon Family Study, Critical Reviews in Analytical Chemistry 46(6) (2016) 502-520.

[44] Y. Tian, J. Wu, A comprehensive analysis of the BET area for nanoporous materials, AIChE Journal 64(1) (2017) 286-293.

[45] M. Lawrence, Y. Jiang, Porosity, Pore Size Distribution, Micro-structure, in: S. Amziane, F. Collet (Eds.), Bio-aggregates Based Building Materials : State-of-the-Art Report of the RILEM Technical Committee 236-BBM, Springer Netherlands, Dordrecht, 2017, pp. 39-71.

[46] F.R. Earle, C.H. Vanetten, T.F. Clark, I.A. Wolff, Compositional data on sunflower seed, Journal of the American Oil Chemists' Society 45(12) (1968) 876-879.

[47] P. Cancalon, Chemical composition of sunflower seed hulls, Journal of the American Oil Chemists' Society 48(10) (1971) 629.

[48] Z.Q. Wen, L.D. Barron, L. Hecht, Vibrational Raman optical activity of monosaccharides, J. Am. Chem. Soc. 115(1) (1993) 285-292.

[49] N.A. Nikonenko, D.K. Buslov, N.I. Sushko, R.G. Zhbankov, Investigation of stretching vibrations of glycosidic linkages in disaccharides and polysaccharides with use of IR spectra deconvolution, Biopolymers 57(4) (2000) 257-262.

[50] L. Pasqua, F. Testa, R. Aiello, Interfacial polycondensation of mesoporous silica particles at the nanometer scale, in: J. Čejka, N. Žilková, P. Nachtigall (Eds.), Studies in Surface Science and Catalysis, Elsevier2005, pp. 557-564.

[51] S.-H. Wu, C.-Y. Mou, H.-P. Lin, Synthesis of mesoporous silica nanoparticles, Chem. Soc. Rev. 42(9) (2013) 3862-3875.

[52] T.C. Sindhu Kanya, B.R. Lokesh, M.C. Shamanthaka Sastry, EFFECT OF SUNFLOWER WAX SUPPLEMENTED DIET ON LIPID PROFILES IN ALBINO RATS, Journal of Food Biochemistry 32(1) (2008) 60-71.

[53] A. Viveros, L.T. Ortiz, M.L. Rodríguez, A. Rebolé, C. Alzueta, I. Arija, C. Centeno, A. Brenes, Interaction of dietary high-oleic-acid sunflower hulls and different fat sources in broiler chickens, Poultry Science 88(1) (2009) 141-151.

[54] Y. Sun, K. Ma, T. Kao, K.A. Spoth, H. Sai, D. Zhang, L.F. Kourkoutis, V. Elser, U. Wiesner, Formation pathways of mesoporous silica nanoparticles with dodecagonal tiling, Nature Communications 8(1) (2017) 252.

[55] D. Niu, Z. Ma, Y. Li, J. Shi, Synthesis of Core–Shell Structured Dual-Mesoporous Silica Spheres with Tunable Pore Size and Controllable Shell Thickness, Journal of the American Chemical Society 132(43) (2010) 15144-15147.

[56] M.C. Ribas, M.A. Adebayo, L.D.T. Prola, E.C. Lima, R. Cataluña, L.A. Feris, M.J. Puchana-Rosero, F.M. Machado, F.A. Pavan, T. Calvete, Comparison of a homemade cocoa shell activated carbon with commercial activated carbon for the removal of reactive violet 5 dye from aqueous solutions, Chemical Engineering Journal 248 (2014) 315-326.

[57] S.C. Smith, D.F. Rodrigues, Carbon-based nanomaterials for removal of chemical and biological contaminants from water: A review of mechanisms and applications, Carbon 91 (2015) 122-143.

[58] D.A. Giannakoudakis, G.Z. Kyzas, A. Avranas, N.K. Lazaridis, Multi-parametric adsorption effects of the reactive dye removal with commercial activated carbons, J. Mol. Liq. 213 (2016) 381-389.

[59] I. Langmuir, THE ADSORPTION OF GASES ON PLANE SURFACES OF GLASS, MICA AND PLATINUM, J. Am. Chem. Soc. 40(9) (1918) 1361-1403.

[60] L.S. Campbell, B.E. Davies, Soil sorption of caesium modelled by the Langmuir and Freundlich isotherm equations, Applied Geochemistry 10(6) (1995) 715-723.

[61] H. Freundlich, H. Hatfield, Colloid [and] capillary chemistry, Methuen, London, 1926.

[62] N. Kannan, M.M. Sundaram, Kinetics and mechanism of removal of methylene blue by adsorption on various carbons—a comparative study, Dyes and Pigments 51(1) (2001) 25-40.

[63] P. Shinde, S.S. Gupta, B. Singh, V. Polshettiwar, B.V. Prasad, Amphi-functional mesoporous silica nanoparticles for dye separation, Journal of Materials Chemistry A 5(28) (2017) 14914-14921.

[64] S. Kachbouri, N. Mnasri, E. Elaloui, Y. Moussaoui, Tuning particle morphology of mesoporous silica nanoparticles for adsorption of dyes from aqueous solution, Journal of Saudi Chemical Society (2017).

[65] P. Qin, Y. Yang, X. Zhang, J. Niu, H. Yang, S. Tian, J. Zhu, M. Lu, Highly Efficient, Rapid, and Simultaneous Removal of Cationic Dyes from Aqueous Solution Using Monodispersed Mesoporous Silica Nanoparticles as the Adsorbent, Nanomaterials 8(1) (2018) 4.

[66] Y. Zhang, F. Gao, B. Wanjala, Z. Li, G. Cernigliaro, Z. Gu, High efficiency reductive degradation of a wide range of azo dyes by SiO2-Co core-shell nanoparticles, Applied Catalysis B: Environmental 199 (2016) 504-513.

[67] M. Li, Y. Yao, W. Zhang, J. Zheng, X. Zhang, L. Wang, Fractionation and Concentration of High-Salinity Textile Wastewater using an Ultra-Permeable Sulfonated Thin-film Composite, Environ. Sci. Technol. 51(16) (2017) 9252-9260.

[68] S. Thakur, M.S. Chauhan, Treatment of Dye Wastewater from Textile Industry by Electrocoagulation and Fenton Oxidation: A Review, in: V.P. Singh, S. Yadav, R.N. Yadava (Eds.) Water Quality Management, Springer Singapore, Singapore, 2018, pp. 117-129.

[69] F. Abiri, N. Fallah, B. Bonakdarpour, Sequential anaerobic–aerobic biological treatment of colored wastewaters: case study of a textile dyeing factory wastewater, Water Sci. Technol. 75(6) (2017) 1261.

[70] J. Qiu, Y. Feng, X. Zhang, M. Jia, J. Yao, Acid-promoted synthesis of UiO-66 for highly selective adsorption of anionic dyes: Adsorption performance and mechanisms, J. Colloid Interface Sci. 499 (2017) 151-158.

[71] S.K. Das, M.M.R. Khan, T. Parandhaman, F. Laffir, A.K. Guha, G. Sekaran, A.B. Mandal, Nano-silica fabricated with silver nanoparticles: antifouling adsorbent for efficient dye removal, effective water disinfection and biofouling control, Nanoscale 5(12) (2013) 5549-5560.

[72] P. Banerjee, S.R. Barman, A. Mukhopadhayay, P. Das, Ultrasound assisted mixed azo dye adsorption by chitosan–graphene oxide nanocomposite, Chemical Engineering Research and Design 117 (2017) 43-56.

[73] M. Jamshidi, M. Ghaedi, K. Dashtian, A.M. Ghaedi, S. Hajati, A. Goudarzi, E. Alipanahpour, Highly efficient simultaneous ultrasonic assisted adsorption of brilliant green and eosin B onto ZnS nanoparticles loaded activated carbon: Artificial neural network modeling and central composite design optimization, Spectrochimica Acta Part A: Molecular and Biomolecular Spectroscopy 153 (2016) 257-267.

[74] C.-H. Tsai, W.-C. Chang, D. Saikia, C.-E. Wu, H.-M. Kao, Functionalization of cubic mesoporous silica SBA-16 with carboxylic acid via one-pot synthesis route for effective removal of cationic dyes, J. Hazard. Mater. 309 (2016) 236-248.

[75] M. Wawrzkiewicz, M. Wiśniewska, V.M. Gun'ko, V.I. Zarko, Adsorptive removal of acid, reactive and direct dyes from aqueous solutions and wastewater using mixed silica–alumina oxide, Powder Technology 278 (2015) 306-315.

[76] R. Zambare, X. Song, S. Bhuvana, J.S. Antony Prince, P. Nemade, Ultrafast Dye Removal Using Ionic Liquid–Graphene Oxide Sponge, ACS Sustainable Chemistry & Engineering 5(7) (2017) 6026-6035.

[77] S. Jayanthi, N. KrishnaRao Eswar, S.A. Singh, K. Chatterjee, G. Madras, A.K. Sood, Macroporous three-dimensional graphene oxide foams for dye adsorption and antibacterial applications, RSC Advances 6(2) (2016) 1231-1242.

[78] W. Song, B. Gao, X. Xu, L. Xing, S. Han, P. Duan, W. Song, R. Jia, Adsorption–desorption behavior of magnetic amine/Fe3O4 functionalized biopolymer resin towards anionic dyes from wastewater, Bioresour. Technol. 210 (2016) 123-130.

[79] D. Dutta, D. Thakur, D. Bahadur, SnO2 quantum dots decorated silica nanoparticles for fast removal of cationic dye (methylene blue) from wastewater, Chemical Engineering Journal 281 (2015) 482-490.

[80] M.G. Torres, S.V. Muñoz, A.R. Martínez, V.S. Hernández, A.V. Saucedo, E.R. Cervantes, R.R. Talavera, M. Rivera, M. del Pilar Carreón Castro, Morphology-controlled silicon oxide particles produced by red wiggler worms, Powder Technology 310 (2017) 205-212.

[81] J.A.A. J¨²nior, J.o.B. Baldo, The Behavior of Zeta Potential of Silica Suspensions, New Journal of Glass and Ceramics Vol.04No.02 (2014) 9.

[82] E.J. Kwon, M. Skalak, A. Bertucci, G. Braun, F. Ricci, E. Ruoslahti, M.J. Sailor, S.N. Bhatia, Porous Silicon Nanoparticle Delivery of Tandem Peptide Anti-Infectives for the Treatment of Pseudomonas aeruginosa Lung Infections, Advanced Materials 29(35) (2017) 1701527-n/a.

[83] L. Li, W. Gu, J. Liu, S. Yan, Z.P. Xu, Amine-functionalized SiO2 nanodot-coated layered double hydroxide nanocomposites for enhanced gene delivery, Nano Research 8(2) (2015) 682-694.

[84] Y. Wang, Y. Sun, J. Wang, Y. Yang, Y. Li, Y. Yuan, C. Liu, Charge-Reversal APTES-Modified Mesoporous Silica Nanoparticles with High Drug Loading and Release Controllability, ACS Applied Materials & Interfaces 8(27) (2016) 17166-17175.

[85] F.M. Hassan, V. Chabot, J. Li, B.K. Kim, L. Ricardez-Sandoval, A. Yu, Pyrrolic-structure enriched nitrogen doped graphene for highly efficient next generation supercapacitors, Journal of Materials Chemistry A 1(8) (2013) 2904-2912.

[86] Q. Lv, W. Si, J. He, L. Sun, C. Zhang, N. Wang, Z. Yang, X. Li, X. Wang, W. Deng, Y. Long, C. Huang, Y. Li, Selectively nitrogen-doped carbon materials as superior metal-free catalysts for oxygen reduction, Nature Communications 9(1) (2018) 3376.

[87] X. Wang, G. Sun, P. Routh, D.-H. Kim, W. Huang, P. Chen, Heteroatom-doped graphene materials: syntheses, properties and applications, Chem. Soc. Rev. 43(20) (2014) 7067-7098.

[88] G. Guan, J. Xia, S. Liu, Y. Cheng, S. Bai, S.Y. Tee, Y.-W. Zhang, M.-Y. Han, Electrostatic-Driven Exfoliation and Hybridization of 2D Nanomaterials, Advanced Materials 29(32) (2017) 1700326-n/a.

[89] J. Gregory, Chapter 3 - Floc formation and floc structure, in: G. Newcombe, D. Dixon (Eds.), Interface Science and Technology, Elsevier2006, pp. 25-43.

[90] Z. Souguir, A.-L. Dupont, J.-B. d'Espinose de Lacaillerie, B. Lavédrine, H. Cheradame, Chemical and Physicochemical Investigation of an Aminoalkylalkoxysilane As Strengthening Agent for Cellulosic Materials, Biomacromolecules 12(6) (2011) 2082-2091.

33

[91] R.M. Pasternack, S. Rivillon Amy, Y.J. Chabal, Attachment of 3-(Aminopropyl)triethoxysilane on Silicon Oxide Surfaces: Dependence on Solution Temperature, Langmuir 24(22) (2008) 12963-12971.

[92] M. Kind, Colloidal aspects of precipitation processes, Chem. Eng. Sci. 57(20) (2002) 4287-4293.

[93] V. Srivastava, D. Gusain, Y.C. Sharma, Critical Review on the Toxicity of Some Widely Used Engineered Nanoparticles, Ind. Eng. Chem. Res. 54(24) (2015) 6209-6233.

[94] V. Subramaniyam, S.R. Subashchandrabose, P. Thavamani, M. Megharaj, Z. Chen, R. Naidu, Chlorococcum sp. MM11—a novel phyco-nanofactory for the synthesis of iron nanoparticles, Journal of Applied Phycology 27(5) (2015) 1861-1869.

[95] J. Jang, H.G. Hur, M.J. Sadowsky, M.N. Byappanahalli, T. Yan, S. Ishii, Environmental Escherichia coli: ecology and public health implications—a review, Journal of Applied Microbiology 123(3) (2017) 570-581.

[96] P. Saravanan, K. Jayamoorthy, S. Ananda Kumar, Design and characterization of non-toxic nano-hybrid coatings for corrosion and fouling resistance, Journal of Science: Advanced Materials and Devices 1(3) (2016) 367-378.

[97] K.P. Miller, L. Wang, B.C. Benicewicz, A.W. Decho, Inorganic nanoparticles engineered to attack bacteria, Chem. Soc. Rev. 44(21) (2015) 7787-7807.

Silanol

Plant Extract

APTES

Hydrothermal Treatment

Dialysis Purification

Positively Charged Porous Silanol Nanoparticles
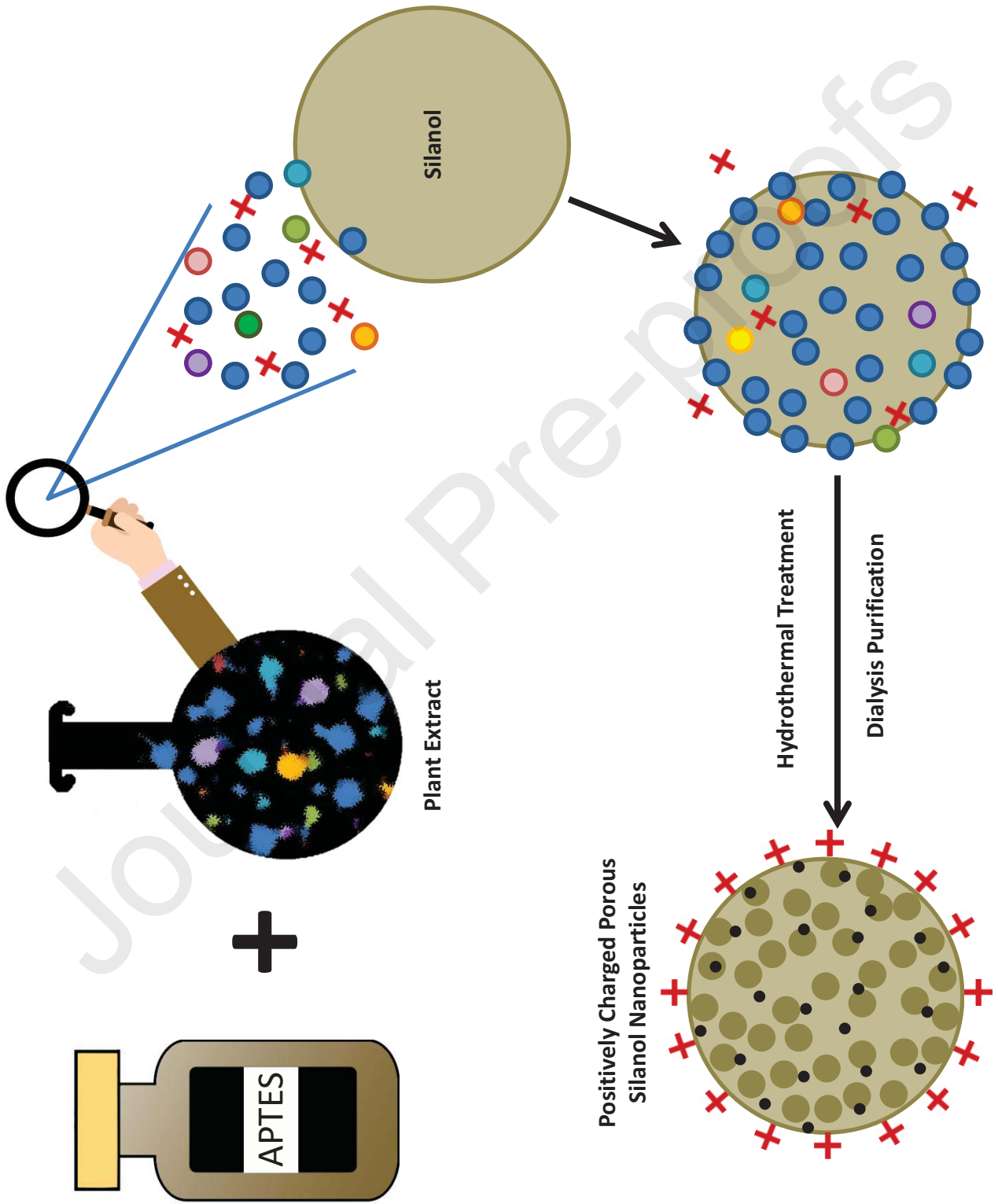
Declaration of interests

☒ The authors declare that they have no known competing financial interests or personal relationships that could have appeared to influence the work reported in this paper.

☒The authors declare the following financial interests/personal relationships which may be considered as potential competing interests:

with permission and on behalf of all the authors)

35